Erschienen in: Journal of the American Chemical Society ; 144 (2022), 30. - S. 13704-13716
https://dx.doi.org/10.1021/jacs.2c04516

Exploring Structure–Property Relations of B,S-Doped Polycyclic Aromatic Hydrocarbons through the Trinity of Synthesis, Spectroscopy, and Theory

Tao Jin, Lukas Kunze, Stefanie Breimaier, Michael Bolte, Hans-Wolfram Lerner, Frieder Jäkle, Rainer F. Winter, Markus Braun, Jan-Michael Mewes,* and Matthias Wagner*

ABSTRACT: Polycyclic aromatic hydrocarbons (PAHs) are prominent lead structures for organic optoelectronic materials. This work describes the synthesis of three B,S-doped PAHs with heptacene-type scaffolds via nucleophilic aromatic substitution reactions between fluorinated arylborane precursors and 1,2-$(Me_3SiS)_2C_6H_4$/1,8-diazabicyclo[5.4.0]undec-7-ene (72–92% yield). All compounds contain tricoordinate B atoms at their 7,16-positions, kinetically protected by mesityl (Mes) substituents. PAHs **1**/**2** feature two/four S atoms at their 5,18-/5,9,14,18-positions; PAH **3** is a 6,8,15,17-tetrafluoro derivative of **2**. For comparison, we also prepared the skewed naphtho[2,3-*c*]-pentaphene-type isomer **4**. The simultaneous presence of electron-accepting B atoms and electron-donating S atoms results in a redox-ambiphilic behavior; the radical cations $[\mathbf{1}^{\bullet}]^+$ and $[\mathbf{2}^{\bullet}]^+$ were characterized by electron paramagnetic resonance spectroscopy. Several low-lying charge-transfer states exist, some of which (especially S-to-B and Mes-to-B transitions) compete on the excited-state potential-energy surface. Consistent with the calculated state characters and oscillator strengths, this competition results in a spread of fluorescence quantum yields (2–27%). The optoelectronic properties of **1** change drastically upon addition of Ag^+ ions: while the color of **1** in CH_2Cl_2 changes bathochromically from yellow to red (λ_{max} from 463 to 486 nm; −0.13 eV), the emission band shifts hypsochromically from 606 to 545 nm (+0.23 eV), and the fluorescence quantum yield increases from 12 to 43%. According to titration experiments, higher order adducts $[Ag_n\mathbf{1}_m]^{n+}$ are formed. As a suitable system for modeling Ag^+ complexation, our calculations predict a dimer structure ($n = m = 2$) with Ag_2S_4 core, approximately linear S–Ag–S fragments, and Ag–Ag interaction. The computed optoelectronic properties of $[Ag_2\mathbf{1}_2]^{2+}$ agree well with the experimentally observed ones.

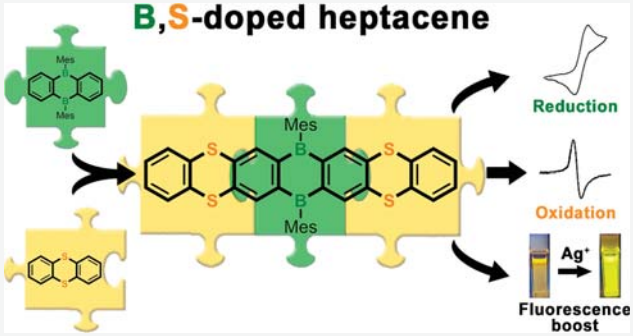

INTRODUCTION

The incorporation of p-block heteroatoms into polycyclic aromatic hydrocarbons (PAHs) is a versatile approach to create new materials for applications in organic optoelectronic devices.[1] In particular, doping with B atoms (B-PAHs) can lead to highly sought-after *n*-type semiconductors, because the presence of formally vacant B(p_z) orbitals in a π-conjugated system tends to lower the energy of the lowest unoccupied molecular orbital (LUMO), which can therefore readily accept an injected electron. In turn, doping with π-donating N, O, or S atoms (N-, O-, or S-PAHs) can provide p-type semiconductor components that are easily oxidized due to their high-energy highest occupied molecular orbitals (HOMOs). Furthermore, the interplay between π-acceptor and π-donor atoms within the same PAH often leads to charge-transfer (CT) transitions upon photoexcitation. In other cases, appropriately designed B,N- and B,O-PAHs exhibit *multiple resonance effects* that induce significant localization of the HOMOs and LUMOs on different sets of C atoms and thereby produce blue thermally activated delayed fluorescence with extremely narrow linewidths.[2]

Electrophilic aromatic substitution protocols (S_EAr) are becoming increasingly popular for the introduction of B atoms into PAHs.[3] Pre-installed electron-rich N, O, or S atoms promote the borylation reaction and, in addition, can be exploited as directing groups in the synthesis of *ortho*-substituted arylboranes, which are otherwise difficult to access.[3] The late-stage N, O, or S doping of PAHs is possible through nucleophilic substitution reactions (S_NAr) on aryl fluorides—especially if these contain mesomerically electron-withdrawing

Konstanzer Online-Publikations-System (KOPS)
URL: http://nbn-resolving.de/urn:nbn:de:bsz:352-2-10w9mbmc4i6do9

Scheme 1. Synthesis of Compounds 1−4 and Crystallographically Determined Solid-State Structures of Compounds 2, 3, and 4[a]

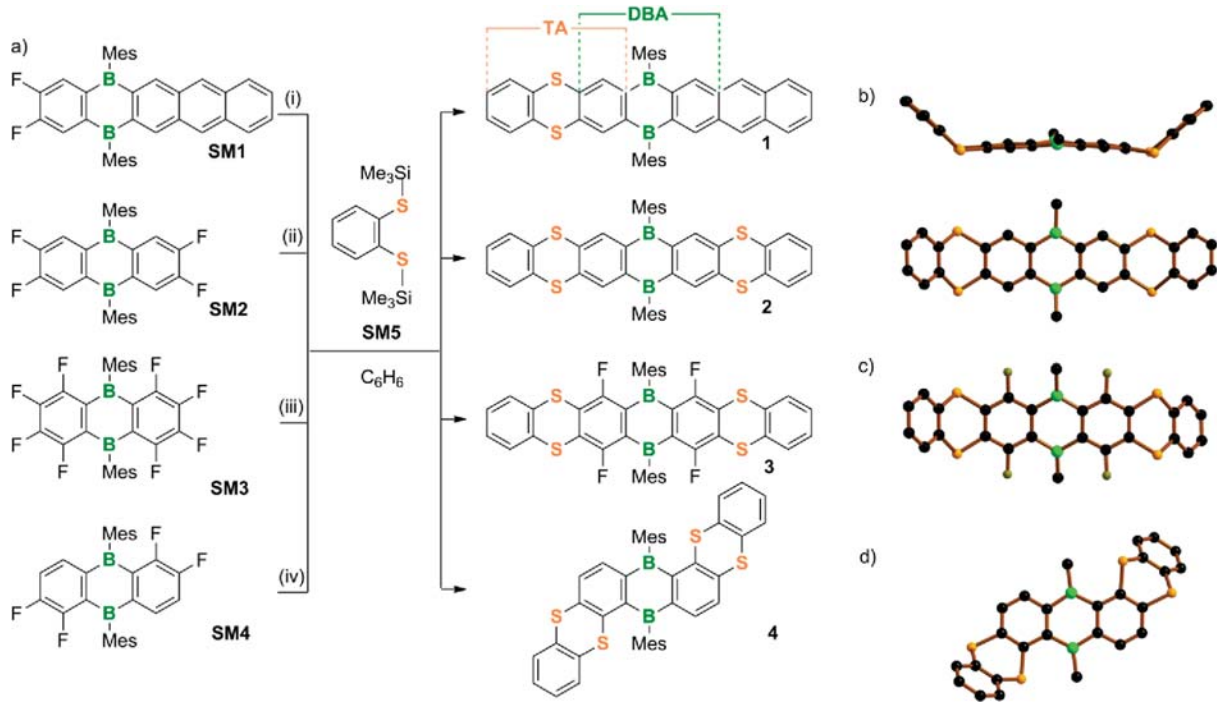

[a](a) Synthesis of B,S-PAHs **1−4** through DBU-catalyzed S_NAr reactions (DBU = 1,8-diazabicyclo[5.4.0]undec-7-ene). (i) 180 °C, 1 d, 80 mol % DBU relative to **SM1**; yield: 82%. (ii) 100 °C, 12 h, 30 mol % DBU relative to **SM2**; yield: 92%. (iii) 130 °C, 1 d, 30 mol % DBU relative to **SM3**; yield: 72%. (iv) 130 °C, 2 d, 30 mol % DBU relative to **SM4**; yield: 74%. (b) Solid-state structure of **2**; top: side view to show the cis bending, bottom: top view. (c) Solid-state structure of **3** (trans bent). (d) Solid-state structure of **4** (trans bent). H atoms and all mesityl-C atoms (except the *ipso* atoms C_i) have been omitted for clarity; B: green, C: black, F: yellow-green, S: orange spheres.

auxiliary substituents.[4,5] Boryl groups would in principle be suitable candidates for this function, but the highly polar solvents usually required to stabilize the Meisenheimer-type reaction intermediates [*e.g.*, dimethylformamide (DMF), dimethyl sulfoxide, *N*-methyl-2-pyrrolidone, and hexamethylphosphoramide] are strong Lewis bases and difficult to obtain in an anhydrous form, which renders them incompatible with most arylboranes. The problem is aggravated by the tendency of N, O, or S nucleophiles to attack not only the Ar−F moiety but also the Lewis-acidic B atom, thereby triggering undesired side reactions. As a consequence, S_NAr reactions on B-PAHs have rarely been described.[6] Herein, we will show that a carefully optimized S_NAr protocol, relying on the silylated sulfur reagent 1,2-$(Me_3SiS)_2C_6H_4$, the organocatalyst 1,8-diazabicyclo[5.4.0]-undec-7-ene (DBU), and the solvent C_6H_6, provides a high-yield synthesis of B,S-PAHs.

We focused on the heptacene scaffold because it is an important lead structure for the development of organic optoelectronic materials.[7] Our target B,S-doped PAHs with heptacene-type scaffolds **1−4** (Scheme 1) can be regarded as hybrids of 9,10-dihydro-9,10-diboraanthracenes (DBAs) and thianthrenes (TAs), both of which are prominent structural motifs in organic electronic materials.[8] With the aim of developing strong PAH-derived electron acceptors, our group has recently prepared a systematic series of fluorinated DBAs and investigated how the fluorine load and topological placement enhance their propensity for one- and two-electron reduction.[9] These compounds are now also available as ideally suited starting materials for (partial) S_NAr derivatizations (**SM1−SM4**; Scheme 1). TAs have long been known for their ability to form persistent $[TA^{\bullet}]^+$-radical salts (*cf.* the small-gap semiconductor $[TA][PF_6]$),[10] which constitute valuable and strong organic oxidants.[11] Moreover, neutral TAs may act as S-donor ligands toward Ag^+ ions.[12] The ambipolar compounds **1−4** are therefore of interest not only for their electronically communicating S and B atoms but also because they should respond to three easily applied external stimuli: reduction/oxidation, UV/vis irradiation, and Ag^+-ion addition. A comparison of **1** and **2** provides insights into the effects of different degrees of S doping, while the couples **2**/**3** and **2**/**4** reveal how introduced F atoms and a skewed PAH framework influence the optoelectronic properties of B,S-PAHs.

RESULTS AND DISCUSSION

Synthesis and Structural Characterization of B,S-PAHs. The required fluorinated B-PAH starting materials **SM1−SM4** (Scheme 1a) are readily available via well-established synthetic routes;[9,13] the S_NAr reaction protocol was optimized for **SM2**. Initially, we adopted the reaction conditions reported by Ong and Swager for the synthesis of extended redox-active TAs from *ortho*-aryldithiols and *ortho*-aryldifluorides (exc. K_2CO_3, 1:1 tetrahydrofuran (THF)/DMF, 120 °C, 3 d).[14] However, already upon addition of DMF to a mixture of neat **SM2**/1,2-$(HS)_2C_6H_4/K_2CO_3$ at room temperature, the characteristic pale yellow color of **SM2** immediately faded, and NMR spectroscopy indicated the formation of a complex mixture of compounds. Heating the sample at 120 °C for 3 d resulted in even more side products. This outcome was not surprising, as our extensive experience with DBAs[1c] shows that they do not tolerate treatment with Brønsted bases, especially if HO- or HS-containing reactants are present.[15] We

therefore switched from 1,2-$(HS)_2C_6H_4$ to the protected arylsulfide nucleophile 1,2-$(Me_3SiS)_2C_6H_4$ (**SM5**)[16] and activated it *in situ* with DBU (Scheme 1a).[17] Because **SM5** is less polar than 1,2-$(HS)_2C_6H_4$, the reaction could now be carried out in the chemically more innocent solvent C_6H_6,[18] and the release of Me_3SiF also provides a thermodynamic thrust to drive the S_NAr reaction to completion.[19] Although our approach requires similarly forcing conditions as Swager's protocol to form two to four aryl–S bonds, the yields obtained are consistently high (72–92%).

According to NMR spectroscopy, the conversions to **1**–**4** are essentially quantitative. Compound **2** is poorly soluble in C_6H_6, so it already crystallizes from the reaction mixture and can be purified by an effortless washing step in an excellent yield of 92%. Purification of **1** requires repeated column chromatography, which slightly lowers the yield (82%). Chromatographic workup is not an option for the air- and moisture-sensitive products **3** and **4**; instead, they were purified by recrystallization (72 and 74% yield, respectively). The higher sensitivity of **3** compared to **2** is likely attributable to its four F substituents, which increase the Lewis acidity of the B centers. This is also reflected by cyclic voltammetry measurements and quantum-chemical calculations, which uniformly indicate that the LUMO energy of **3** is indeed lower than that of **2**.[20] The higher sensitivity of **4** compared to **2** is less straightforward to explain because the reduction potentials (see below) and computed LUMO energies/electron affinities of both compounds are essentially identical.[20] However, we already encountered a comparable situation when we found that 6,13-dimesityl-6,13-dihydro-6,13-diborapentacene is significantly less Lewis acidic than a related compound featuring two biphenylene-2,3-diyl units in place of naphthalene-2,3-diyl moieties.[21]

Another remarkable finding is the high selectivity of the reaction of **SM3** toward the linear B,S-PAH **3**, because the successful synthesis of the skewed B,S-PAH **4** shows that the F atoms in *peri* positions to the Mes groups are also susceptible to substitution. Because the synthesis of **4** requires significantly higher temperatures and longer reaction times than the synthesis of the less sterically hindered **2** (Scheme 1a), we assume that steric factors contribute to the selectivity of the formation of **3**. Furthermore, the known dynamic and self-correcting nature of the S_NAr reactions employed here[14] should help to ensure that any sterically encumbered "false" C–S connections are isomerized, ultimately affording only the linear compound **3**.

All NMR spectra were recorded at room temperature in CD_2Cl_2. The ^{11}B NMR resonances of **1**–**4** appear in the range of 62–76 ppm, testifying to the presence of tricoordinate B atoms.[22] In the ^1H NMR spectra, the integral ratios between the Mes signals and the resonances of the 1,2-$S_2C_6H_4$ fragments show that one and two such moieties were successfully introduced into **1** and **2**–**4**, respectively. This conclusion is further supported by the fact that **1**, **2**, and **4** no longer give rise to ^{19}F NMR signals. Compound **3** shows one singlet at $\delta(^{19}F)$ = −97 ppm, in line with an average D_{2h} symmetry of this B,S-PAH. Parent TA is non-planar and folded about the S···S vector by a dihedral angle of 131° (gas-phase measurement)[23] or 128° (X-ray diffraction).[24] Yet, the inversion barrier is low (5.3 kcal mol^{-1}),[25] and in solution, TA flips rapidly through a planar conformation, which explains why we found no indication for the presence of cis/trans isomers in the NMR spectra of **2**–**4** (the computed inversion barriers of **1**–**4** also fall within the narrow range of 3.1–6.3 kcal mol^{-1}).[20] The ^{13}C NMR resonances of **1**–**4** were fully assigned with the help of 2D NMR experiments.

The proposed molecular structures of **2**–**4** were confirmed by single-crystal X-ray diffraction. As expected, all three molecules deviate from planarity in the solid state, with **2** adopting a cis conformation of the two terminal phenylene rings (Scheme 1b), while **3** and **4** are trans bent (Scheme 1c,d).[20] According to quantum-chemical calculations, the energies of corresponding cis and trans conformers are equal within the accuracy of the method.

Experimentally Determined Optoelectronic Properties of B,S-PAHs. UV/vis absorption and emission spectra of **1**–**4** were measured in C_6H_6 and CH_2Cl_2 (Figure 1a; more polar solvents, such as MeCN or DMF, are strong Lewis bases that tend to interact with the B centers).[26] The longest-wavelength maxima in the UV/vis absorption spectra are λ_{max} = 463 nm (2.68 eV; **1**), 388 nm (3.20 eV; **2**), 421 nm (2.95 eV; **3**), and 484 nm (2.56 eV; **4**), which fits to the computed values (CH_2Cl_2, Tables 1 and S7 and Figure 1b).[20] The switch from a linear to a skewed framework (**2** *vs* **4**) thus has a substantially larger impact on λ_{max} than the introduction of four F-atom substituents (**2** *vs* **3**).

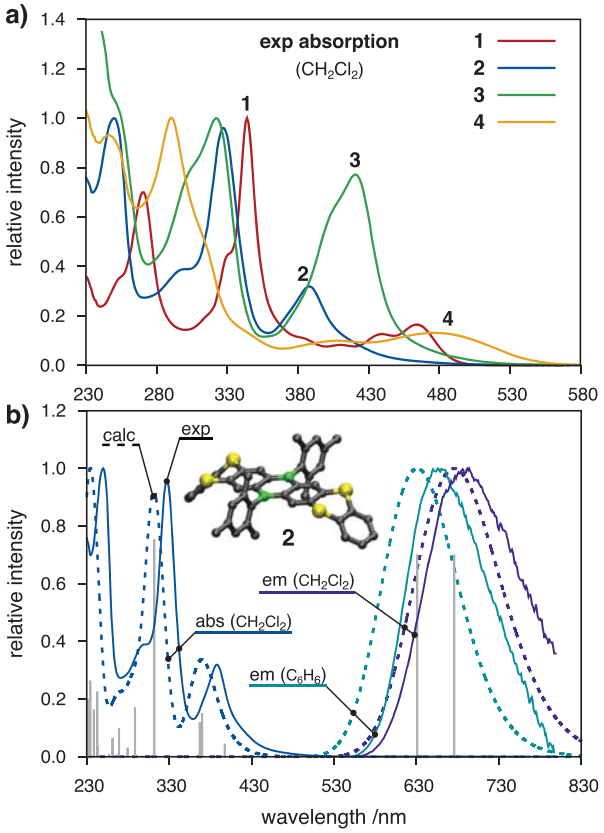

Figure 1. (a) Normalized UV/vis absorption spectra of **1**–**4** in CH_2Cl_2. (b) Comparison of calculated (dotted lines) and experimental (solid lines) spectra of **2** (absorption in CH_2Cl_2: blue; emission in CH_2Cl_2: violet; emission in C_6H_6: blue-green). Intensities are relative and have been normalized to 1.0 for the highest completely visible peak in each spectrum. Level of theory for absorption: OT-LRC-ωPBEh/def2-TZVPP//r^{2}SCAN-3c with pt(SS + LR)-PCM solvation, for emission: OT-LRC-ωPBEh/def2-TZVPP//def2-SVP with state-specific-polarizable continuum solvation model (SS-PCM) solvation.

Table 1. Photophysical and Electrochemical Data of Compounds 1−4[a]

	λ_{abs} [nm] (ε [M^{-1} cm^{-1}])[b]	λ_{ex} [nm]	λ_{em} [nm]	Φ_{PL} [%][c]	E_{HOMO}/E_{LUMO} [eV][d]	$E_{1/2}$ [V]	E_G^{cv} [eV][e]
1	253 (sh)	345	606	12	−5.69/−2.93	−1.87	2.76
	271 (95,800)		585[f]	16[f]		0.89	
	330 (sh)						
	345 (133,100)						
	386 (sh)						
	412 (sh)						
	440 (17,200)						
	463 (22,500)						
2	250 (65,400)	250	692	6	−5.79/−3.19	−1.61	2.60
	301 (26,100)		658[f]	11[f]		0.90/0.99	
	328 (62,300)						
	388 (21,000)						
	420 (sh)						
3	324 (61,600)	325	697	2	-[g]/−3.48	−1.32	
	421 (48,000)		668[f]	6[f]			
4	292 (58,800)	290	709	11	-[g]/−3.19	−1.61	
	410 (sh)		673[f]	27[f]			
	484 (7600)						

[a]Optical and electrochemical measurements were performed in CH_2Cl_2 and $CH_2Cl_2/[n\text{Bu}_4\text{N}][PF_6]$ (0.1 M), respectively. [b]Absorption data acquired in C_6H_6 or 1,2-$C_2H_4Cl_2$ are listed in the Supporting Information (Tables S1 and S2); sh = shoulder. [c]Quantum yields were determined by using a calibrated integrating sphere. [d]$E_{HOMO} = -4.8\text{ eV} - E_{1/2}^{Ox}$, $E_{LUMO} = -4.8\text{ eV} - E_{1/2}^{Red}$ (FcH/FcH$^+$ = −4.8 eV *vs* vacuum level). [e]Electrochemically determined band gap. [f]The measurements were performed in C_6H_6. [g]Compound shows no reversible oxidation. λ_{abs}: absorption maxima, λ_{em}: emission maximum, λ_{ex}: excitation wavelength.

All four B,S-PAHs **1**−**4** are photoluminescent with emission wavelengths of λ_{em} = 606 (2.05 eV; **1**), 692 (1.79 eV; **2**), 697 (1.78 eV; **3**), and 709 nm (1.75 eV; **4**; CH_2Cl_2, Table 1), which are well reproduced by our quantum-chemical calculations (Figure 1b, Table S7).[20] Again, the effect of structural isomerism (**2** *vs* **4**) is more pronounced than that of the introduction of four F atoms (**2** *vs* **3**). Moreover, we observe (i) low to moderate quantum yields of Φ_{PL} = 2−12% (CH_2Cl_2), and (ii) an increase in the Φ_{PL} values to 6−27% accompanied by a marked blue shift of all the emissions upon going from CH_2Cl_2 to C_6H_6 (positive solvatochromism; Table 1). This indicates a higher polarity of the electronically excited state, likely because of the presence of CT, as confirmed by quantum-chemical calculations (see below).[20]

Cyclic voltammograms were recorded for **1**−**4** [CH_2Cl_2, room temperature, supporting electrolyte: $[n\text{Bu}_4\text{N}][PF_6]$ (0.1 M), *versus* FcH/FcH$^+$ (FcH = ferrocene); Table 1].[20] All four compounds undergo reversible one-electron reduction, at $E_{1/2}$ = −1.87 (**1**), −1.61 (**2**), −1.32 (**3**), and −1.61 V (**4**). Thus, an increasing number of incorporated S atoms (**1** *vs* **2**) and the introduction of F-atom substituents (**2** *vs* **3**) facilitate electron uptake, while skewing the linear framework of **2** (as in **4**) has no measurable effect on the reduction potential. Compound **1** presents a chemically partially reversible anodic redox wave at $E_{1/2}$ = 0.89 V. Compound **2** presents two overlapping, likewise partially reversible waves for the stepwise oxidations of the individual TA subunits. Half-wave potentials were retrieved from the peak-to-peak separation of the composite wave and the peak width of the forward anodic wave as 0.90 and 0.99 V, according to the method of Richardson and Taube.[27] Compounds **3** and **4** were irreversibly oxidized so that no half-wave potentials can be provided. The oxidation potential of parent TA ($E_{1/2}$ = 0.90 V,[11,28] 0.85 V;[10] MeCN, *vs* FcH/FcH$^+$) compares well with those of **1** and **2**, which indicates that the B atoms do not withdraw significant charge density from the S atoms.[29]

In an attempt to experimentally probe the identity of the "redox-orbitals" HOMO and LUMO, which are primarily involved in the oxidation or reduction processes, we resorted to *in situ* UV/vis and electron paramagnetic resonance (EPR) spectroscopy through spectroelectrochemical (SCE) experiments.[20] Compound **2** was chosen as a representative example.[30] Thianthrenium radical cations have a characteristic vis absorption band near 550 nm (*e.g.*, 543 nm for parent $[TA^{\bullet}]^+$).[31] Electrolytic oxidation of **2** in an optically transparent thin-layer electrolysis cell[32] at room temperature resulted in (partial) bleaching of the prominent near-UV/vis bands of **2**, but the typical bands of a $[TA^{\bullet}]^+$ radical cation were not detected (Table S2, Figure S14). Despite the presence of isosbestic points at *ca.* 258 and 293 nm, re-reduction produced the initial bands in only 35% spectroscopic yield (Figure S15). We note in this context that the electrochemistry of TA under air- and water-free conditions is complicated by the facts that (i) $[TA^{\bullet}]^+$ is no longer butterfly-shaped but has an essentially planar framework and (ii) reversible dimerization occurs via the S atoms to give $[(TA)_2]^{2+}$ in polar solvents.[12b] It is likely that similar issues arise after the oxidation of **2** as well.

In situ electrolysis of a solution of **2** in $CH_2Cl_2/[n\text{Bu}_4\text{N}][PF_6]$ at −40 °C gave an isotropic EPR signal at g = 1.9903 for $[\mathbf{2}^{\bullet}]^+$, which is somewhat smaller than g = 2.008 for the pristine $[TA^{\bullet}]^+$ radical cation[28,33] but still shows that a radical species was generated. No hyperfine coupling to the H atoms on the adjacent phenyl rings is resolved (Figure S16), which, according to the density functional theory (DFT) calculations outlined below, can be explained by line broadening due to unresolved coupling to two quadrupolar $^{10/11}$B nuclei (similar EPR results as for $[\mathbf{2}^{\bullet}]^+$ were obtained for the $[\mathbf{1}^{\bullet}]^+$ radical cation of **1**[20]).

The reversible reduction of **2** allowed us to also monitor the spectroscopic changes accompanying the **2** → $[\mathbf{2}^{\bullet}]^-$ reduction process. Our results show partial bleaching of all UV/vis bands of **2**, the concomitant growth of a new structured vis band with discernible peaks at 584 and 631 nm, and clean isosbestic

points.[34] Subsequent re-oxidation regenerated the initial spectrum with a high optical yield, which confirms our assignment of these bands to the $[\mathbf{2}^{\bullet}]^{-}$ radical anion (Figure S14, Table S2).

Boosting the Fluorescence of 1 by Ag^+ Addition. As mentioned above, compounds **1**–**4** are only moderately luminescent (Table 1). We therefore wondered whether the emission properties could be improved by coordinating metal ions to the S atoms of our B,S-PAHs. Particularly one booster effect is conceivable: the CT character of the transitions arising from the TA donor(s) should decrease, because metal–S coordination lowers the energy of the lone pairs at the S atoms, which are otherwise natural electron-donor sites.

For the complexation studies, compound **1** was selected as the prospective ligand because it contains only two S-atom donors. We chose the salt $Ag[Al\{OC(CF_3)_3\}_4]$ for our complexation studies because it is readily soluble in non-donor solvents such as CH_2Cl_2, the extremely weakly coordinating "teflonate" counter anion should not compete with **1** for the Ag^+ ions,[35] and the Ag^+ ion is naked and does not carry spectator ligands. Several $[Ag_n(TA)_m]^{n+}$ complexes are known and were structurally characterized.[12] It was found that one TA ligand can coordinate either one Ag^+ ion in a chelating η^2 mode or two Ag^+ ions simultaneously in a κ^2-*S*,*S*′ mode. The resulting Ag^+/TA stoichiometries were 1:1 or 2:3; there is a tendency toward formation of oligonuclear aggregates. In addition to forming Ag–S bonds, the Ag^+ cation can also interact with π electrons of an *ortho*-phenylene ring of a second TA molecule.

In view of this intricate constellation, it was not clear from the outset in which ratio **1** and $Ag[Al\{OC(CF_3)_3\}_4]$ should be combined. We therefore performed Ag^+-titration experiments in CD_2Cl_2/CH_2Cl_2 and monitored the progress of the reaction by NMR, UV/vis, and emission spectroscopy.

During the Ag^+ titration, the ^1H NMR spectra revealed appreciable downfield shifts for the protons in *ortho*- and *meta*-positions to the S atoms ($\Delta\delta$ = 0.36–0.43), while all other proton signals shifted by less than 0.05 ppm (Figure S29). This points to an interaction of the Ag^+ ions with the TA part of **1** and corroborates the previously inferred interaction of Ag^+ with the HOMO of **1** via the S atoms.[12a] Most of the changes occur in the range of 0–1.5 equiv of added Ag^+; gradually increasing the amount of Ag^+ further to a total of 6 equiv had little additional effect, indicating tight binding of Ag^+ to the ligand **1** with a high binding constant.

Already the naked-eye observation of the titration mixture revealed a color change from yellow (free ligand **1**) to orange (**1** + 0.5 equiv Ag^+) and finally to bright red (**1** + ≥1 equiv Ag^+; Figure 2). In the UV/vis spectrum, the longest-wavelength absorption shifted bathochromically from λ_{max} = 463 to 486 nm, a new band emerged at 295 nm, and the two prominent absorptions of free **1** at 271 and 345 nm decreased (Figure 2). At least four isosbestic points are visible at 245, 280, 315, and 470 nm, indicating that most likely only two species, that is, free ligand **1** and one specific Ag^+ complex of **1**, contribute to the absorption. Again, most of the changes in the UV/vis spectrum of the titration mixture occurred in the range of 0–1.5 equiv of Ag^+. In the presence of a vast excess of Ag^+ (15 equiv), only the new band at 295 nm showed some further increase, while the intensities of all other bands remained essentially unchanged (relative to the state after 1.5 equiv Ag^+ had been added). The reversibility of Ag^+ complexation was demonstrated by two further experiments carried out with a sample of **1** + 1.5 equiv Ag^+: (i) Dilution of one aliquot of the sample with the same volume of pure CH_2Cl_2 gave a similar spectrum as previously observed after addition of 0.5 equiv of Ag^+ during titration of **1** (Figure 2). (ii) When the mixture was back-titrated with $[n\mathrm{Bu}_4\mathrm{N}]Cl$, the original UV/vis spectrum of free **1** was recovered after 1.5 equiv of the chloride salt had been added (Figure S32).

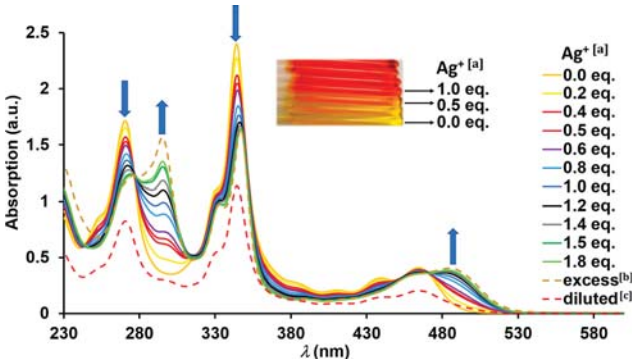

Figure 2. UV/vis absorption spectra recorded during the titration of **1** with $Ag[Al\{OC(CF_3)_3\}_4]$ in CH_2Cl_2; the inset shows the visual color change of CH_2Cl_2 solutions of **1** in the presence of various amounts of Ag^+ ions. [a] Total amount of $Ag[Al\{OC(CF_3)_3\}_4]$ in the sample. [b] Stoichiometric ratio between $Ag[Al\{OC(CF_3)_3\}_4]$ and **1** was approximately 15:1. [c] For this measurement, an aliquot of the sample at the titration end point was diluted with the same volume of pure CH_2Cl_2.

Global fits of the UV/vis absorption data for the titration of **1** with $Ag[Al\{OC(CF_3)_3\}_4]$ in CH_2Cl_2 were performed using 70 different wavelengths over the range of λ = 260 to 510 nm (HypSpec software).[36] Based on these fits, we considered two scenarios: scenario 1—immediate formation of one single complex; scenario 2—successive formation of monomeric or dimeric complexes. Scenario 1: the formation of $[Ag\mathbf{1}_2]^+$ or of $[Ag_2\mathbf{1}]^+$ as the only complex in the solution can be excluded. Similarly, an attempt to describe the data with a simple 1:1 model, in which $[Ag\mathbf{1}]^+$ appears as the sole complex, gave a poor fit (Figure S34). The data fit relatively better to formation of a higher order 2:2 complex ($[Ag_2\mathbf{1}_2]^{2+}$) with an association constant $\lg(\beta_{22})$ of approximately 14.7 (Figure S35). Scenario 2: The possibility of step-wise processes with intermediate formation of complex $[Ag\mathbf{1}_2]^+$ *en route* to $[Ag_2\mathbf{1}_2]^{2+}$ was also examined (Figure S37). A good fit was obtained assuming that Ag^+ ions are bridging two ligands in the system ($\mathbf{1}/[Ag\mathbf{1}_2]^+/[Ag_2\mathbf{1}_2]^{2+}$) [$\lg(\beta_{12})$ = 10.7, $\lg(\beta_{22})$ = 15.8]. This scenario explains the rapid and almost linear change in absorbance at the beginning of the titration and the tapering-off after adding >1 equiv Ag^+. It is also consistent with a still incomplete complex formation at 1.8 equiv Ag^+, as indicated by the still increasing absorbance at λ = 295 nm when an excess amount of 15 equiv Ag^+ is added. A fit to a 3:2 complex ($[Ag_2\mathbf{1}_3]^{2+}$) gave an association constant $\lg(\beta_{32})$ of approximately 18.7 (Figure S36). However, the most important finding to highlight is that all of these scenarios essentially postulate the formation of higher order complexes $[Ag_n\mathbf{1}_m]^{n+}$ rather than a simple monomeric 1:1 complex $[Ag\mathbf{1}]^+$.[37] In these complexes, the Ag^+ ions are assumed to adopt bridging positions between ligands **1**, consistent with the earlier structural data of related Ag^+ complexes of TA.[12] Further, the large values of the binding constants derived from the data fitting indicate that the Ag^+ ions interact strongly with ligand **1**.

The proposed composition of the complex between Ag^+ and **1** in CH_2Cl_2 was further examined by means of a Job's plot.[38] For this purpose, we mixed a total of 10 aliquots of two equimolar stock solutions of $Ag[Al\{OC(CF_3)_3\}_4]$ and **1** in a cuvette and diluted each mixture to a volume of 3.1 mL. This way, the total concentration of the two components was kept constant, while the Ag^+/**1** ratio varied systematically from sample to sample. The absorbances A of the samples at the wavelength where the change of the optical density of free and complexed **1** is maximal (λ = 345 nm) were determined. Finally, the deviation of A from the theoretically expected value A_{ligand} was calculated for the ligand concentration present in each sample ($\Delta A = A_{ligand} - A$). Plotting the ΔA values of all samples against the mole fractions of Ag^+ (χ_{Ag}) gave a bell-shaped curve (Figures S38 and S39), indicating a 2:2 or higher order n/m complex between the metal and ligand,[20,37] consistent with the results from titration data fitting (see above) and computational studies (see below).[39]

When viewed under UV irradiation (λ_{ex} = 366 nm), successive Ag^+ addition causes a color change of the luminescence from red (free ligand **1**) to green (**1** + ≥0.5 equiv Ag^+; Figure 3). In line

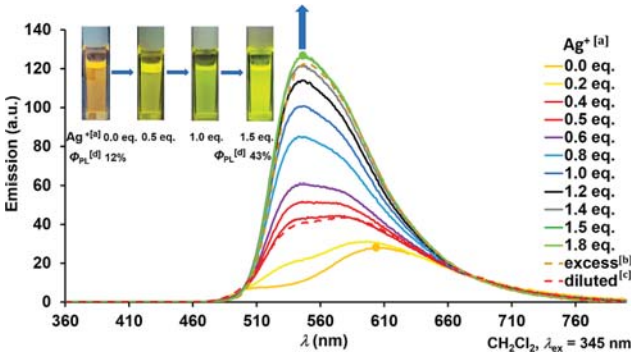

Figure 3. Emission spectra recorded during titration of **1** with $Ag[Al\{OC(CF_3)_3\}_4]$ in CH_2Cl_2. [a] Total amount of $Ag[Al\{OC(CF_3)_3\}_4]$ in the sample. [b] Stoichiometric ratio between $Ag[Al\{OC(CF_3)_3\}_4]$ and **1** was approximately 15:1. [c] For this measurement, an aliquot of the sample at the titration end point was diluted with the same volume of pure CH_2Cl_2. [d] Quantum yields were determined by using a calibrated integrating sphere. Note: The orange and green discs mark the maxima of the respective curves; the shoulder at the hypsochromic slope of the orange curve is due to a highly emissive impurity (probably unconsumed starting material **SM1**).

with that, the position of the emission maximum shifts from 606 nm (**1**) to 545 nm (**1** + ≥1 equiv Ag^+; λ_{ex} = 345 nm). Most importantly, an increase in the Ag^+ content of the sample causes an increase in the fluorescence quantum yield from Φ_{PL} = 12 to 43%, which comes to a halt after 1.5 equiv of Ag^+ have been added. Note: The shoulder observed in the emission spectrum of **1** at shorter wavelengths is due to a minor contamination (most likely starting material **SM1**) and not due to dual emission; it does not affect the reported results.[40] As already discussed for the UV/vis experiments, back-titration with $[n Bu_4N]Cl$ restores the original emission spectrum of **1** (see Figure S33), and diluting the sample **1** + 1.5 equiv Ag^+ shifts the emission maximum back to where it was after the addition of approximately 0.4 equiv Ag^+.

We finally measured the emission lifetimes of the free ligand **1** and of 1:1 or 2:1 mixtures of $Ag[Al\{OC(CF_3)_3\}_4]$ and **1** by the time-correlated single photon counting (TCSPC) method after optical excitation at 325 nm (CH_2Cl_2; Figure 4). The emission signal of the free ligand **1** decays mono-exponentially with a

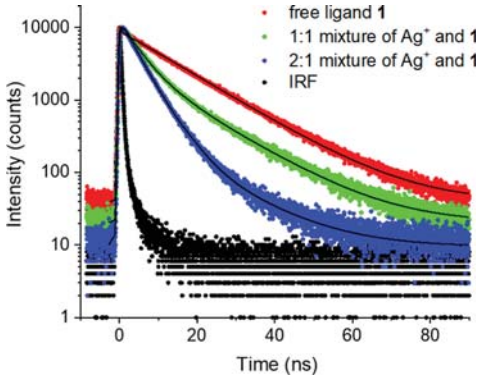

Figure 4. Emission-decay curves recorded by the TCSPC method for the free ligand **1** (red dots) and for 1:1 (green dots) or 2:1 (blue dots) mixtures of $Ag[Al\{OC(CF_3)_3\}_4]$ and **1** (CH_2Cl_2). The emission was optically excited at 325 nm (instrument response function shown as black dots). Theoretical decay curves from a bi-exponential fit procedure are shown as black lines.

lifetime τ_1 = 13.5 ns. The emission–decay curves of the mixtures containing Ag^+ ions show a bi-exponential behavior for both the 1:1 mixture [τ_1 = 13.5 ns (51%), τ_2 = 4.1 ns (49%)] and the 2:1 mixture [τ_1 = 13.4 ns (11%), τ_2 = 4.1 ns (89%); percentage values given in parentheses refer to the fractional intensities]. The lifetime component τ_1 is associated with the unconsumed ligand **1**, while the component τ_2 is attributed to the excited-state decay of the $[Ag_n\mathbf{1}_m]^{n+}$ complex. This confirms the existence of a dynamic association–dissociation equilibrium m **1** + n $Ag^+ \leftrightharpoons [Ag_n\mathbf{1}_m]^{n+}$, which is shifted toward the formation of $[Ag_n\mathbf{1}_m]^{n+}$ if an excess of Ag^+ ions is present. In the case of a static equilibrium (associated with irreversible complex formation), the 2:1 mixture would be expected to exhibit monoexponential decay with a lifetime of 4.1 ns. The lifetime measurements lead to the following conclusion: The emission-boosting effect of Ag^+ is not due to a switch from fluorescence to phosphorescence because (i) the emission wavelength of the Ag^+ complex(es) is shorter than that of free **1** and (ii) the emission lifetime decreases significantly upon Ag^+ complexation. Moreover, the TCSPC data give radiative decay rates $k_r = \Phi/\tau$ of 8.9×10^6 s^{-1} for the free ligand **1** and of 104.9×10^6 s^{-1} for $[Ag_n\mathbf{1}_m]^{n+}$. This corresponds to a relative enhancement by a factor of 12, which is in good qualitative agreement with the computed enhancement of the corresponding oscillator strengths (factor of 25).

To further interpret the experimentally obtained results and to gain deeper insights into the electronic structures of our compounds, we explored their ground and excited states through DFT and time-dependent DFT (TDDFT) calculations. These calculations address three central questions: (i) What is the nature of the low-lying excited states of **1**–**4** at the Franck–Condon point and for emission? (ii) Do the computed EPR spectra of $[\mathbf{1}^\bullet]^+$ and $[\mathbf{2}^\bullet]^+$ support the assumption that these species were generated in the course of our SCE studies? (iii) How does Ag^+ coordination influence the CT in compound **1** regarding the change in color and the increase in Φ_{PL}?

TDDFT Analysis of Low-Lying Excited States of 1–4. We conducted TDDFT calculations[41] with the optimally tuned range-separated functional OT-LRC-ωPBEh.[42] This choice is motivated by the fact that range separation, combined with non-empirical optimal tuning, substantially improves the TDDFT description of CT states, which are present in all four molecules (see the Supporting Information for further details). To account for the strong influence of solvation effects on absorption and

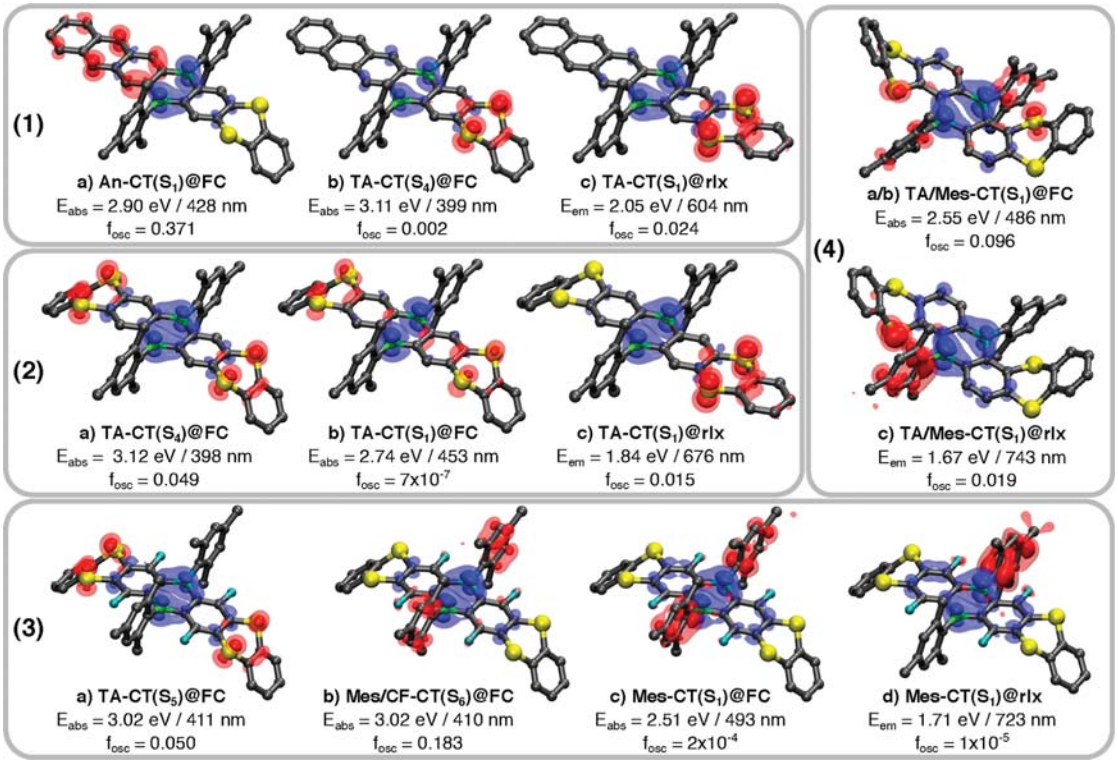

Figure 5. Electron difference-density plots for selected excited states of compounds **1**−**4**. These include the energetically lowest visible excited states (**1a**−**4a**) at the Franck−Condon point (@FC, *i.e.*, at the ground-state optimized structure), those photoexcited states at the FC point that subsequently relax into the emitting states (1b, 2b, 3c, 4b), and the emitting states at their relaxed optimized structures (@rlx; 1c, 2c, 3d, 4c). The difference between the latter two structures shows the effect of excited-state optimization (*e.g.*, the vanishing kink in **1** and **2** and a localization of CT states in **3** and **4**). Note that for **3**, an additional state is shown, while (4a,4b) are the same state. Isosurfaces are drawn at isovalues of 0.006 a.u. (opaque) and 0.024 a.u. (transparent) and have been calculated at the OT-LRC-ωPBEh/def2-TZVPP//r^{2}SCAN-3c level of theory with pt(SS + LR)-PCM solvation for absorption and OT-LRC-ωPBEh/def2-TZVPP//def2-SVP level of theory for emission (further details are provided in the Supporting Information); red and blue surfaces show electron density decrease and increase, respectively.

emission energies as well as on the character of polar CT states, we use a SS-PCM for ground and excited states in the equilibrium and non-equilibrium formalism, namely, the SS-PCM and perturbative pt(SS + LR)-PCM.[43]

The CT character found for the low-lying excited states of **1**−**4** can be traced back to the combination of the energetically low-lying acceptor orbital, the LUMO (dominated by the vacant B(p_z) orbitals), and the following donor moieties: the TA-embedded S atoms (TA-CT), the 2,3-anthrylene fragment (An-CT),[21] the B-bonded mesityl substituents (Mes-CT),[21] and the difluorophenylene ring (CF-CT). In addition, we identified several hybrid CT excited states that arise if energy levels and structural features allow mixing between pure CT states. Hybrid CT states are denoted as, for example, TA/Mes-CT for a TA-CT and Mes-CT hybrid. The computed lowest-energy absorptions of **1**−**4** that are associated with sufficiently high oscillator strengths (f_{osc}) to be detectable in the experimental UV/vis spectra are discussed in detail below, along with the emitting states. Dark states up to energies of approximately 4 eV, which do not contribute to the absorption spectrum, are discussed briefly. All states and transitions were calculated in CH_2Cl_2. A comprehensive overview of energies, f_{osc}, and characters of all low-lying states in CH_2Cl_2 is given in Table S7; a visualization of the most relevant excited states (difference densities of the lowest absorbing and emitting states, the latter at the ground state and its relaxed structure) is displayed in Figure 5. A discussion and visualization of all excited states (including those with f_{osc} values below the experimental threshold) is provided in the Supporting Information (Figures S49−S52). In general, there is remarkable quantitative agreement between the experimental and computed spectra (see Figures 1, 7, S45−S48 and Tables 1, S7, and S8).[44]

For compound **1**, the lowest excited singlet state (S_1) is an An-CT state (2.90 eV/428 nm; 1a in Figure 5),[45] while a TA-CT state (S_4) has a slightly higher energy (3.11 eV/399 nm; 1b in Figure 5). Due to very small overlap between the excitation hole in the nonbonding lone pairs at the S atoms and the excited electron in the B(p_z) orbitals, the TA-CT state has a small f_{osc} = 0.002 and, accordingly, negligible absorption. In contrast, the An-CT state has a much larger overlap between the hole in the 2,3-anthrylene π system and the adjacent B(p_z) orbitals, leading to f_{osc} = 0.371. In addition to these bright states, there are several pure Mes-CT states (S_2, S_5, S_6, S_7, and S_9) between 3.05 eV/406 nm and 3.78 eV/328 nm, that is, near the second strong absorption band. However, these states are not visible in the spectrum due to their vanishing f_{osc} [all <0.005; see Figure S45 (spectra) and Figure S49 (difference densities)]. The second strong absorption is due to S_{10} 3.80 eV/326 nm (f_{osc} = 1.431), which appears to be a mixture of local excitation of the 2,3-anthrylene fragment and some TA-CT character. The emitting state of **1** is the TA-CT state (S_4 at the ground-state structure, also called Franck−Condon point), which moves more than 0.5 eV below the An-CT and Mes-CT states in the relaxed regime, that is, when the structures are optimized on the respective

excited-state potential-energy surface. The computed vertical emission energy of the TA-CT state is 2.05 eV/604 nm with f_{osc} = 0.024 (1c in Figure 5), corresponding to a more than 10-fold increase in f_{osc} compared to the corresponding excited state at ground-state geometry. The particularly strong energetic stabilization and increase of f_{osc} of the relaxed TA-CT state is a result of large structural changes in the excited-state optimization, during which the kink at the S atoms vanishes, leading to a planar π system with a larger overlap and accordingly higher f_{osc} (compare 1b and 1c in Figure 5).

For compound **2**, the three energetically lowest excited singlet states are calculated at energies of 2.74 eV/453 nm, 2.84 eV/437 nm, and 2.98 eV/416 nm. The lowest of these (S_1) is a TA-CT state, while the other two (S_2, S_3) are of Mes-CT character. All three states have only very small oscillator strengths (f_{osc} < 0.005) and are therefore not visible in the spectrum but become relevant for emission (see below). The energetically lowest visible absorption results in a weak band at 3.12 eV/398 nm (f_{osc} = 0.049, S_4; 2a in Figure 5), which is assigned to a pure TA-CT state. The first major peak is predicted at 3.35 eV/370 nm (f_{osc} = 0.175, S_6) and stems from a hybrid TA/Mes-CT transition. It is followed by an unusually bright Mes-CT state at 3.38 eV/367 nm (f_{osc} = 0.139).[20] The next higher excited states are S_8−S_{10} at 3.61 eV/343 nm, 3.98 eV/312 nm, and 4.01 eV/309 nm; all of them have TA-CT character, with varying relative contributions of acceptor and donor orbitals. Of these, only S_9 has a large f_{osc} = 0.870. The computed fluorescence of **2** has an energy of 1.84 eV/676 nm (f_{osc} = 0.015; 2c in Figure 5). Similar to **1**, the emitting state of **2** possesses TA-CT character. It derives from S_1 at the ground-state structure (not detectable in the UV/vis spectrum due to its low f_{osc} value of <0.005)[20] but localizes on one side of the molecule during the relaxation. Accordingly, this side is planarized, whereas the kink on the other side remains (compare 2b and 2c in Figure 5). Analogous to **1**, this leads to a strong stabilization and an increase in f_{osc} to 0.015. Such a Jahn−Teller-like localization is in our experience quite typical for CT states and occurs when symmetry-breaking structural changes are more beneficial than delocalization.[46]

For compound **3**, the four lowest excited singlet states S_1−S_4 lie between 2.51 eV/493 nm and 3.02 eV/411 nm and are all dark with f_{osc} < 0.005. This is a result of their pure CT character (3 × Mes-CT, 1 × TA-CT (S_3); see Figure S47 (spectra) and Figure S51 (difference densities)). The first experimentally detectable absorption peaks are due to S_5 at 3.02 eV/411 nm (f_{osc} = 0.050; 3a in Figure 5), S_6 at 3.02 eV/410 nm (f_{osc} = 0.183; 3b in Figure 5), S_7 at 3.10 eV/400 nm (f_{osc} = 0.287), and S_8 at 3.40 eV/364 nm (f_{osc} = 0.019).[20] The lowest state of **3** leading to a visible absorption (TA-CT, S_5; 3a in Figure 5) is directly related to the lowest visible state of **2** (TA-CT, S_4; 2a in Figure 5), compared to which it is red-shifted due to the four electronegative F substituents that stabilize the electron-accepting LUMO; the f_{osc} values of both states are similar. Both S_6 and S_7 can be characterized as Mes/CF-CT states with different degrees of Mes-CT and CF-CT contributions: for S_6, the donors are mostly the mesitylene units (Mes-CT), while for S_7 and S_8, the electron originates almost equally from the mesitylene (Mes-CT) and difluorophenylene rings (CF-CT). This goes along with a larger electron−hole overlap and explains the larger f_{osc} of S_7. Our calculations predict an emission energy of **3** of 1.71 eV/723 nm and an f_{osc} of only 1 × 10^{-5}, explaining why **3** exhibits the lowest Φ_{PL} of all four compounds. This is due to the different character of the emitting state (Mes-CT) compared to **1** and **2** (TA-CT) and to the fact that the donor (Mes) and acceptor (B_2C_4) planes are essentially orthogonal to each other at the relaxed structure of the emitting state, in which the hole is localized on one of the Mes units (compare 3c *vs* 3d in Figure 5). Moreover, in contrast to **1** and **2**, the lone pairs at the S atoms are not involved in the emitting state, such that **3** retains both kinks at the S_1-relaxed structure of the emitting state.

The ground-state structure of **4** differs from the structures of **1**−**3** by the skewed shape of the π system. As a result, the dihedral angles between the B_2C_4 ring and the Mes substituents deviate by about 10° from the quasi-perpendicular arrangement in **1**−**3**, which allows a higher overlap of the Mes π system with the B(p_z) orbitals and eventually leads to a more pronounced mixing between TA-CT and Mes-CT states (4a/b and 4c in Figure 5). While most of these strongly mixed states do not have oscillator strengths large enough to be visible in the absorption spectrum, S_1 not only attains a substantial f_{osc} of 0.096, but also an excitation energy of 2.55 eV/486 nm, which is distinctly lower than the visible lowest-energy excited states of **1**−**3**. This explains the bathochromically shifted band in the experimental absorption spectra of **4** compared to **1**−**3**. In S_1, the S atoms facing the Mes rings are the predominant donors of both TA units (TA-CT), while the higher-lying CT states up to 4 eV include further mixed states (S_2−S_5), pure Mes-CT (S_6, S_7), and TA-CT states (S_8−S_{10}, see also Figure S52). All of these have relatively low f_{osc} values compared to compounds **1**−**3** (f_{osc} = 0.080 for hybrid S_4, 0.034 and 0.032 for TA-CTs S_8 and S_{10}, respectively; all others <0.01). The emitting state in **4** derives from a TA/Mes-CT (S_1) that is delocalized over both TA/Mes units at the GS structure but localizes on one side of the molecule during the excited-state optimization (compare 4a/b and 4c in Figure 5). The calculated emission energy of 1.67 eV/743 nm is in good agreement with the experiment. The relatively high Φ_{PL} of this state is consistent with the predicted f_{osc} = 0.019, which is as large as the f_{osc} of **1** and much larger than the values calculated for **2** and **3** (Table S7).

DFT Assessment of the Radical Cations $[1^{\bullet}]^+$ and $[2^{\bullet}]^+$. DFT calculations for the radical cations of **1** and **2** were performed with the IGLO-III basis set[47] and the TPSS0 functional,[48] as this showed the best performance of meta-hybrid functionals in a benchmark for hyperfine coupling constants.[49] Moreover, calculated EPR spectra of the parent compound $[TA^{\bullet}]^+$, obtained at the same level of theory, agreed very well with the experimental spectra (Figure S53).[28] Solvent effects were taken into account by the conductor-like polarizable continuum model.

The computed hyperfine coupling constants to the protons on the adjacent phenylene rings do not differ significantly between the radical cations $[1^{\bullet}]^+$ and $[2^{\bullet}]^+$, on the one hand, and $[TA^{\bullet}]^+$, on the other. Using the resulting EPR parameters, we constructed a model spin system with the EasySpin module of MATLAB,[50] with which we conducted our further investigation. This revealed the coupling to the B atoms to be the reason for line broadening. When the B atoms are excluded from the spin system, simulated EPR spectra of both $[1^{\bullet}]^+$ and $[2^{\bullet}]^+$ show coupling patterns similar to that of $[TA^{\bullet}]^+$ (see Figure S54). Inclusion of the B atoms in the spin system creates coupling patterns with small additional hyperfine couplings to the $^{10}B/^{11}B$ nuclei, superimposed on the $[TA^{\bullet}]^+$-like pattern, that cannot be resolved and just lead to signal broadening (see Figure S55).[20]

Complexation of Compound 1 with Ag^+ Ions. We started our investigation by considering a monomeric complex $[Ag1]^+$, in which one Ag^+ ion bridges the two S atoms of one ligand molecule **1** to form a bent S−Ag−S fragment (Figure 6).

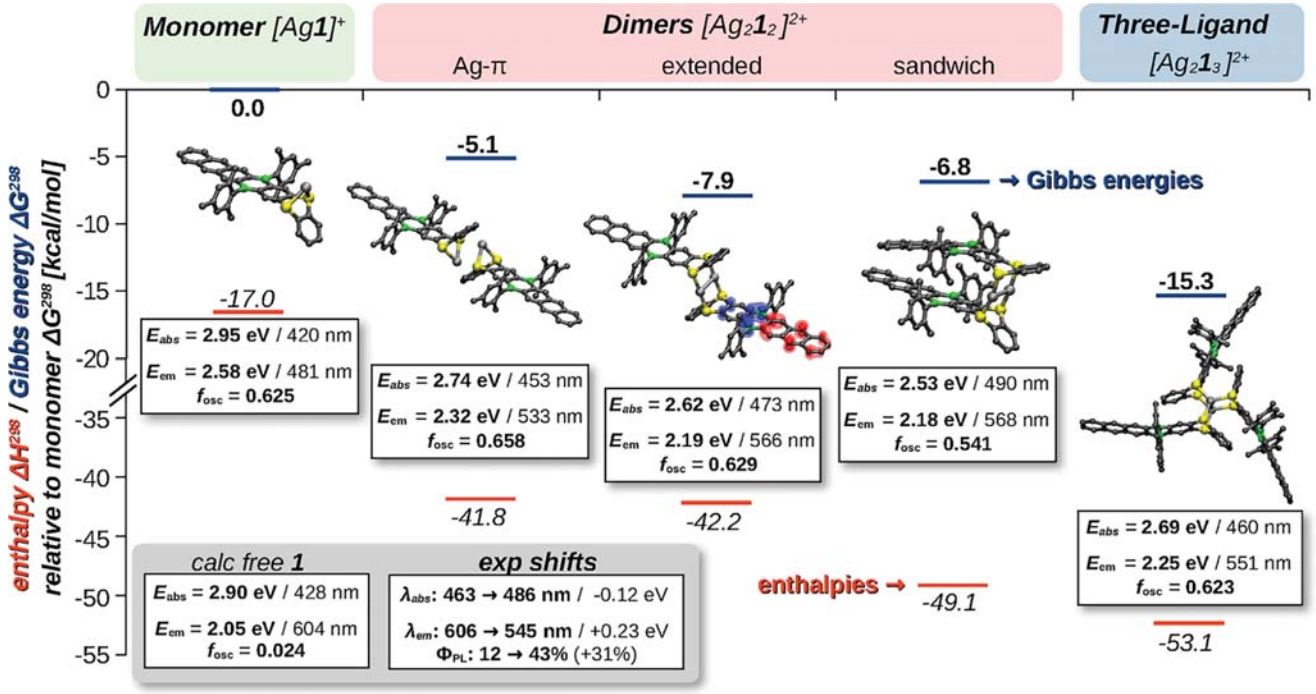

Figure 6. Energy diagram showing the Gibbs energy (blue lines, including entropic contributions) and enthalpy (orange lines, excluding entropic contributions) for the dimerization of the monomeric complex $[Ag\mathbf{1}]^+$ (shaded green) to give the three possible isomers $[Ag_2\mathbf{1}_2]^{2+}$ (shaded red) in CH_2Cl_2. In addition, the three-ligand complex $[Ag_2\mathbf{1}_3]^{2+}$ is included. The optimized (ground-state) structures for all complexes are also shown (H atoms are omitted for clarity; for the extended dimer, we also show the difference density of the emitting state, calculated with the same approach as described for Figure 5). The inlays provide the lowest calculated absorption energies, emission energies (at the excited-state optimized structures), and f_{osc} of emission, all for CH_2Cl_2 solutions. For reference, we also provide the calculated absorption and emission data for free compound **1** and a summary of the experimentally observed changes (gray box at the bottom). Thermochemical calculations were conducted at the revDSD-PBEP86(SMD(CH_2Cl_2))/def2-QZVPP//r^{2}SCAN-3c level of theory (def2-TZVPP for the three-ligand complex), excited-state calculations at the OT-LRC-ωPBEh(IEF-PCM(CH_2Cl_2))/def2-SVP level.[20]

However, computations of the absorption spectra of $[Ag\mathbf{1}]^+$ revealed that the chelating coordination of Ag^+ leads to a significant inhibition of charge transfer from the TA moiety to the B_2C_4 ring, causing a blue shift in the computed longest-wavelength absorption band from 2.90 eV/428 nm in **1** to 2.95 eV/420 nm in $[Ag\mathbf{1}]^+$ (see Figure 7 for a comparison of calculated absorption and emission energies). Because this is in contrast to the experimentally observed red shift of this band from 463 to 486 nm upon Ag^+ addition (Figure 2), we next considered the formation of $[Ag_2\mathbf{1}_2]^{2+}$ dimers and of a three-ligand complex $[Ag_2\mathbf{1}_3]^{2+}$, which turned out to be in much better accord with our experimental Ag^+-titration results. Several different structures are conceivable for these complexes and were found as local minimum structures in a systematic conformer search using the CREST program at the semi-empirical GFN2-xTB level of theory;[51] for all these structures, comparable Ag^+ complexes with other TA ligands exist in the literature,[12a,c] and all of them exhibit a red shift of their lowest absorption band compared to the free ligand. The considered structures include (Figure 6): (i) A dimer, termed "Ag-π", in which two unaltered $[Ag\mathbf{1}]^+$ units bind to each other through intermonomer Ag–π interactions. (ii) An "extended dimer", in which each Ag^+ ion is coordinated to one S atom of each ligand, resulting in two approximately linear S–Ag–S fragments and a near-covalent Ag–Ag interaction, while the 2,3-anthrylene moieties point in opposite directions. (iii) A conformer of the extended dimer with a similar Ag_2S_4 core but with the two 2,3-anthrylene moieties stacked on top of each other, termed "sandwich dimer". (iv) A C_3-symmetric "three-ligand complex" $[Ag_2\mathbf{1}_3]^{2+}$ with a central Ag_2S_6 motif derived from the extended dimer by adding another equivalent of **1**.

To identify the most favorable complexes, final structures, zero-point vibrational energies, and thermostatistical corrections were determined using the r^{2}SCAN-3c composite method[52] for CH_2Cl_2 solutions. Final single-point energies were obtained with a highly accurate double-hybrid density functional in a numerically converged basis set (revDSD-PBEP86-D4[53] with the SMD solvation model[54]).[20] These thermochemical calculations show that at the Gibbs-energy level, the three-ligand cation $[Ag_2\mathbf{1}_3]^{2+}$ is the most stable complex (15.3 kcal mol^{-1} below the monomer) and thus probably a dominant species in solution. The dimers are generally less favorable than $[Ag_2\mathbf{1}_3]^{2+}$ (with Gibbs energies between −5 and −8 kcal mol^{-1}) but nevertheless considerably more stable than the monomer, so they presumably act as intermediates in the formation of $[Ag_2\mathbf{1}_3]^{2+}$. As evident from a comparison of enthalpies (orange bars; Figure 6) and Gibbs energies of formation (blue bars), entropic contributions have a large influence. At the enthalpy level, the sandwich dimer is by far the most favorable dimer and situated only 4 kcal mol^{-1} above $[Ag_2\mathbf{1}_3]^{2+}$. The large difference in free energies between the sandwich dimer and $[Ag_2\mathbf{1}_3]^{2+}$ is thus a result of the entropic contributions favoring the three-ligand complex.[55] We conclude from these thermochemical calculations that "Ag–π" is the least favorable dimer in terms of both enthalpy and Gibbs energy and can thus be excluded from further discussions.[56]

Despite the large size of $[Ag_2\mathbf{1}_3]^{2+}$, it was possible to calculate its full absorption spectrum, emission energy, and large f_{osc} value

(Figure 7). The agreement with the experimental spectra is good for the computed spectrum of $[Ag_2\mathbf{1}_3]^{2+}$, of the extended dimer, and, in part, also of the sandwich dimer (the latter has too little intensity in the high-energy bands; see Figure 7). However, because of their similarity, this comparison of the spectra does not provide further information on which of the complexes is most abundant in solution. Due to the apparent similarity between the calculated absorption and emission of the non-monomeric Ag^+ complexes, we argue that it is justified to use the smaller and thus computationally more tractable extended dimer as representative model system for all complexes in the following discussion of the emission properties.

To explore the reason for the experimentally observed increased Φ_{PL} (43% *vs* 12% for **1**) and blue-shifted emission (545 nm *vs* 606 nm for **1**) upon Ag^+ complexation, we optimized the structures of the complexes for the lowest excited states and compared the calculated f_{osc} values and emission energies with those measured for **1**. The computed f_{osc} increases by more than one order of magnitude upon going from **1** to any of the Ag^+ complexes (*cf.* inlays of Figure 6), explaining their faster and more yielding fluorescence decay.

Inspection of the respective difference density of the energetically lowest relaxed excited state (S_1) of the extended dimer (Figure 6) shows that this is due to a switch in the emitting state compared to free **1**: Ag^+ coordination stabilizes the electron lone pairs on the S atoms to such an extent that the TA-CT state (the emitting state in free **1**) is shifted to significantly higher energies. As a result, the more strongly allowed An-CT state becomes the energetically lowest and thus the emitting state in the complex (free ligand **1**: f_{osc} = 0.588 for An-CT *vs* 0.024 for TA-CT, both at the respective excited-state relaxed structure in CH_2Cl_2; compare also 1a and 1b in Figure 5). Also, the increased emission energy is consistent with such a state switch: The computed emission energy of the An-CT state in free **1** is higher than that of the TA-CT state (free ligand **1**: 2.56 eV/484 nm for An-CT *vs* 2.05 eV/604 nm for TA-CT, both at their relaxed structures in CH_2Cl_2).

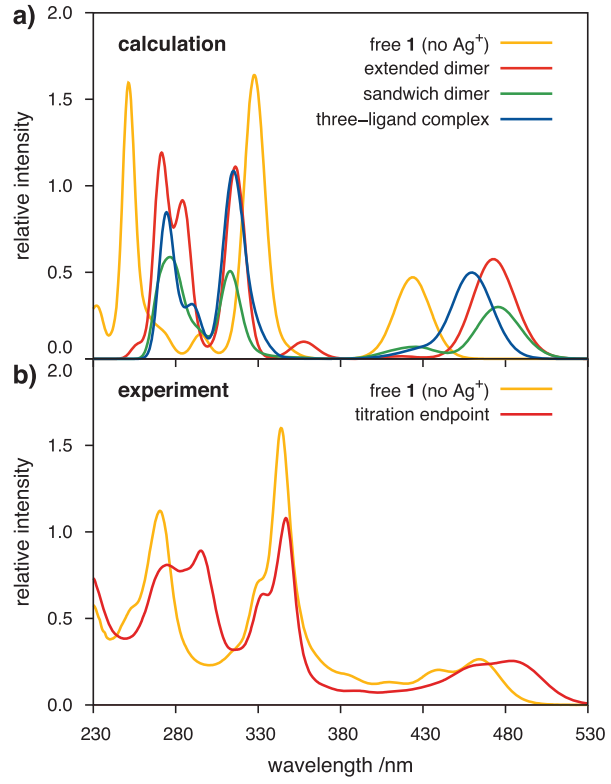

Figure 7. (a) Comparison of the calculated absorption spectra of the free ligand **1** (yellow) and the energetically most favorable Ag^+ complexes extended dimer (red), sandwich dimer (green), and three-ligand complex (blue); all in CH_2Cl_2. (b) Experimentally observed absorption spectra of the free ligand **1** (yellow) and of the reaction mixture at the end point of the titration of **1** with Ag^+ (red; all in CH_2Cl_2). Calculated spectra are obtained by enveloping the first 80 excited singlet states calculated at the OT-LRC-ωPBEh/def2-SVP//r^{2}SCAN-3c level of theory with pt(SS + LR)-PCM solvation with Gaussians with a half-width-full-maximum of 0.2 eV.[20]

CONCLUSIONS

We have synthesized B,S-doped PAHs with heptacene-type scaffolds by largely unexplored but highly efficient nucleophilic aromatic substitution reactions on fluorinated arylboranes. To overcome the problems associated with the notorious base sensitivity of tricoordinate boron species, the silyl-protected nucleophile 1,2-$(Me_3SiS)_2C_6H_4$ was used and activated *in situ* by the catalyst DBU. The products obtained contain electron-accepting DBA moieties annulated to electron-donating TA units and are thus redox ambiphiles. Correspondingly, the UV/vis absorption and emission properties of the compounds are to a large extent governed by S-to-B CT transitions. Quantum-chemical calculations reveal that CT from a TA donor unit is accompanied by drastic structural changes from a folded (along the S···S vector) ground state to a planar excited state. Using 5,18-dithia-7,16-dihydro-7,16-diboraheptacene as the model system, we have shown by experimental and theoretical means that the addition of Ag^+ ions leads to higher order $[Ag_nS_m]^{n+}$ complexes that are 3.5 times more fluorescent than the free ligand (Φ_{PL} = 43% *vs* 12%; CH_2Cl_2); these complexes can be well modeled by a dimer structure $[Ag_2\mathbf{1}_2]^{2+}$. Our newly introduced B,S-doped PAHs thus respond to three different and easily applied triggers: reduction/oxidation, UV/vis irradiation, and Ag^+-ion addition.

ASSOCIATED CONTENT

Supporting Information

The Supporting Information is available free of charge at https://pubs.acs.org/doi/10.1021/jacs.2c04516.

Experimental details and characterization data (PDF)

X-ray crystallographic data (ZIP)

Atomic coordinates of computed molecular structures (XYZ, XYZ)

Accession Codes

CCDC 2167624–2167626 contain the supplementary crystallographic data for this paper. These data can be obtained free of charge via www.ccdc.cam.ac.uk/data_request/cif, or by emailing data_request@ccdc.cam.ac.uk, or by contacting The Cambridge Crystallographic Data Centre, 12 Union Road, Cambridge CB2 1EZ, UK; fax: +44 1223 336033.

AUTHOR INFORMATION

Corresponding Authors

Jan-Michael Mewes − *Mulliken Center for Theoretical Chemistry, Institut für Physikalische und Theoretische Chemie, Universität Bonn, 53115 Bonn, Germany;* orcid.org/0000-0002-4669-8091; Email: janmewes@janmewes.de

Matthias Wagner − *Institut für Anorganische und Analytische Chemie, Goethe-Universität Frankfurt, D-60438 Frankfurt am Main, Germany;* orcid.org/0000-0001-5806-8276; Email: matthias.wagner@chemie.uni-frankfurt.de

Authors

Tao Jin − *Institut für Anorganische und Analytische Chemie, Goethe-Universität Frankfurt, D-60438 Frankfurt am Main, Germany*

Lukas Kunze − *Mulliken Center for Theoretical Chemistry, Institut für Physikalische und Theoretische Chemie, Universität Bonn, 53115 Bonn, Germany*

Stefanie Breimaier − *Fachbereich Chemie, Universität Konstanz, D-78453 Konstanz, Germany*

Michael Bolte − *Institut für Anorganische und Analytische Chemie, Goethe-Universität Frankfurt, D-60438 Frankfurt am Main, Germany;* orcid.org/0000-0001-5296-6251

Hans-Wolfram Lerner − *Institut für Anorganische und Analytische Chemie, Goethe-Universität Frankfurt, D-60438 Frankfurt am Main, Germany;* orcid.org/0000-0003-1803-7947

Frieder Jäkle − *Department of Chemistry, Rutgers University-Newark, Newark, New Jersey 07102, United States;* orcid.org/0000-0001-8031-9254

Rainer F. Winter − *Fachbereich Chemie, Universität Konstanz, D-78453 Konstanz, Germany;* orcid.org/0000-0001-8381-0647

Markus Braun − *Institut für Physikalische und Theoretische Chemie, Goethe-Universität Frankfurt, D-60438 Frankfurt (Main), Germany;* orcid.org/0000-0002-7891-6954

Notes

The authors declare no competing financial interest.

■ ACKNOWLEDGMENTS

We are grateful to the China Scholarship Council for providing a PhD scholarship to T.J. and to the Research Training Group (RTG) 2591 (TIDE) of the Deutsche Forschungsgemeinschaft (DFG) for providing funding for the PhD work of L.K.

■ REFERENCES

(1) (a) *Main Group Strategies towards Functional Hybrid Materials*; Baumgartner, T., Jäkle, F., Eds.; John Wiley & Sons, Ltd.: Chichester, UK, 2017; pp 1−110. (b) Mellerup, S. K.; Wang, S. Boron-Doped Molecules for Optoelectronics. *Trends Chem.* **2019**, *1*, 77−89. (c) von Grotthuss, E.; John, A.; Kaese, T.; Wagner, M. Doping Polycyclic Aromatics with Boron for Superior Performance in Materials Science and Catalysis. *Asian J. Org. Chem.* **2018**, *7*, 37−53. (d) Stępień, M.; Gońka, E.; Żyła, M.; Sprutta, N. Heterocyclic Nanographenes and Other Polycyclic Heteroaromatic Compounds: Synthetic Routes, Properties, and Applications. *Chem. Rev.* **2017**, *117*, 3479−3716. (e) Ji, L.; Griesbeck, S.; Marder, T. B. Recent Developments in and Perspectives on Three-Coordinate Boron Materials: A Bright Future. *Chem. Sci.* **2017**, *8*, 846−863. (f) Yamaguchi, S.; Fukazawa, A.; Taki, M. Phosphole P-Oxide-Containing π-Electron Materials: Synthesis and Applications in Fluorescence Imaging. *J. Synth. Org. Chem., Jpn.* **2017**, *75*, 1179−1187. (g) Escande, A.; Ingleson, M. J. Fused Polycyclic Aromatics Incorporating Boron in the Core: Fundamentals and Applications. *Chem. Commun.* **2015**, *51*, 6257−6274. (h) Hirai, M.; Tanaka, N.; Sakai, M.; Yamaguchi, S. Structurally Constrained Boron-, Nitrogen-, Silicon-, and Phosphorus-Centered Polycyclic π-Conjugated Systems. *Chem. Rev.* **2019**, *119*, 8291−8331.

(2) (a) Hatakeyama, T.; Shiren, K.; Nakajima, K.; Nomura, S.; Nakatsuka, S.; Kinoshita, K.; Ni, J.; Ono, Y.; Ikuta, T. Ultrapure Blue Thermally Activated Delayed Fluorescence Molecules: Efficient HOMO-LUMO Separation by the Multiple Resonance Effect. *Adv. Mater.* **2016**, *28*, 2777−2781. (b) Nakatsuka, S.; Gotoh, H.; Kinoshita, K.; Yasuda, N.; Hatakeyama, T. Divergent Synthesis of Heteroatom-Centered 4,8,12-Triazatriangulenes. *Angew. Chem., Int. Ed.* **2017**, *56*, 5087−5090. (c) Kondo, Y.; Yoshiura, K.; Kitera, S.; Nishi, H.; Oda, S.; Gotoh, H.; Sasada, Y.; Yanai, M.; Hatakeyama, T. Narrowband deep-blue organic light-emitting diode featuring an organoboron-based emitter. *Nat. Photonics* **2019**, *13*, 678−682.

(3) Review articles: (a) Iqbal, S. A.; Pahl, J.; Yuan, K.; Ingleson, M. J. Intramolecular (directed) electrophilic C-H borylation. *Chem. Soc. Rev.* **2020**, *49*, 4564−4591. (b) Bähr, S.; Oestreich, M. The Electrophilic Aromatic Substitution Approach to C-H Silylation and C-H Borylation. *Pure Appl. Chem.* **2018**, *90*, 723−731. (c) Ingleson, M. J. A Perspective on Direct Electrophilic Arene Borylation. *Synlett* **2012**, *23*, 1411−1415. Selected original papers: (d) Iqbal, S. A.; Cid, J.; Procter, R. J.; Uzelac, M.; Yuan, K.; Ingleson, M. J. *Angew. Chem., Int. Ed.* **2019**, *58*, 15381−15385. (e) Crossley, D. L.; Cid, J.; Curless, L. D.; Turner, M. L.; Ingleson, M. J. Facile Arylation of Four-Coordinate Boron Halides by Borenium Cation Mediated Boro-Desilylation and -Destannylation. *Organometallics* **2015**, *34*, 5767−5774. (f) Hirai, H.; Nakajima, K.; Nakatsuka, S.; Shiren, K.; Ni, J.; Nomura, S.; Ikuta, T.; Hatakeyama, T. One-Step Borylation of 1,3-Diaryloxybenzenes Towards Efficient Materials for Organic Light-Emitting Diodes. *Angew. Chem., Int. Ed.* **2015**, *54*, 13581−13585. (g) Matsui, K.; Oda, S.; Yoshiura, K.; Nakajima, K.; Yasuda, N.; Hatakeyama, T. One-Shot Multiple Borylation toward BN-Doped Nanographenes. *J. Am. Chem. Soc.* **2018**, *140*, 1195−1198. (h) Oda, S.; Kumano, W.; Hama, T.; Kawasumi, R.; Yoshiura, K.; Hatakeyama, T. Carbazole-Based DABNA Analogues as Highly Efficient Thermally Activated Delayed Fluorescence Materials for Narrowband Organic Light-Emitting Diodes. *Angew. Chem., Int. Ed.* **2021**, *60*, 2882−2886. (i) De Vries, T. S.; Prokofjevs, A.; Harvey, J. N.; Vedejs, E. Superelectrophilic Intermediates in Nitrogen-Directed Aromatic Borylation. *J. Am. Chem. Soc.* **2009**, *131*, 14679−14687. (j) Prokofjevs, A.; Vedejs, E. N-Directed Aliphatic C-H Borylation Using Borenium Cation Equivalents. *J. Am. Chem. Soc.* **2011**, *133*, 20056−20059. (k) Cazorla, C.; De Vries, T. S.; Vedejs, E. P-Directed Borylation of Phenols. *Org. Lett.* **2013**, *15*, 984−987.

(4) A rare case of a nucleophilic aromatic substitution protocol for B-doping of PAHs is found in: Budy, H.; Prey, S. E.; Buch, C. D.; Bolte, M.; Lerner, H.-W.; Wagner, M. Nucleophilic Borylation of Fluorobenzenes with Reduced Arylboranes. *Chem. Commun.* **2022**, *58*, 254−257.

(5) Amii, H.; Uneyama, K. C−F Bond Activation in Organic Synthesis. *Chem. Rev.* **2009**, *109*, 2119−2183.

(6) Kitamoto, Y.; Suzuki, T.; Miyata, Y.; Kita, H.; Funaki, K.; Oi, S. The First Synthesis and X-Ray Crystallographic Analysis of an Oxygen-Bridged Planarized Triphenylborane. *Chem. Commun.* **2016**, *52*, 7098−7101.

(7) (a) Anthony, J. E. Functionalized Acenes and Heteroacenes for Organic Electronics. *Chem. Rev.* **2006**, *106*, 5028−5048. (b) Payne, M. M.; Parkin, S. R.; Anthony, J. E. Functionalized Higher Acenes: Hexacene and Heptacene. *J. Am. Chem. Soc.* **2005**, *127*, 8028−8029. (c) Einholz, R.; Bettinger, H. F. Heptacene: Increased Persistence of a 4n+2 π-Electron Polycyclic Aromatic Hydrocarbon by Oxidation to the 4n π-Electron Dication. *Angew. Chem., Int. Ed.* **2013**, *52*, 9818−9820. (d) Einholz, R.; Fang, T.; Berger, R.; Grüninger, P.; Früh, A.; Chassé, T.; Fink, R. F.; Bettinger, H. F. Heptacene: Characterization in Solution, in the Solid State, and in Films. *J. Am. Chem. Soc.* **2017**, *139*, 4435−4442. (e) Hayashi, H.; Hieda, N.; Yamauchi, M.; Chan, Y. S.; Aratani, N.; Masuo, S.; Yamada, H. Visible-Light-Induced Heptacene Generation under Ambient Conditions: Utilization of Single-crystal Interior as an Isolated Reaction Site. *Chem.—Eur. J.* **2020**, *26*, 15079−15083.

(8) DBAs: (a) Reus, C.; Weidlich, S.; Bolte, M.; Lerner, H.-W.; Wagner, M. C-Functionalized, Air- and Water-Stable 9,10-Dihydro-

9,10-diboraanthracenes: Efficient Blue to Red Emitting Luminophores. *J. Am. Chem. Soc.* **2013**, *135*, 12892−12907. (b) John, A.; Bolte, M.; Lerner, H.-W.; Meng, G.; Wang, S.; Peng, T.; Wagner, M. Doubly Boron-Doped Pentacenes as Emitters for OLEDs. *J. Mater. Chem. C* **2018**, *6*, 10881−10887. (c) Radtke, J.; Schickedanz, K.; Bamberg, M.; Menduti, L.; Schollmeyer, D.; Bolte, M.; Lerner, H.-W.; Wagner, M. Selective Access to Either a Doubly Boron-Doped Tetrabenzopentacene or an Oxadiborepin from the Same Precursor. *Chem. Sci.* **2019**, *10*, 9017−9027. (d) Kirschner, S.; Uecker, I.; Bolte, M.; Lerner, H.-W.; Wagner, M. How π Extension or Structural Bending Alters the Properties of Boron-Doped Phenylene-Containing Oligoacenes. *Organometallics* **2019**, *38*, 2818−2823. (e) Kumar, A.; Shin, H. Y.; Lee, T.; Jung, J.; Jung, B. J.; Lee, M. H. Doubly Boron-Doped TADF Emitters Decorated with *ortho*-Donor Groups for Highly Efficient Green to Red OLEDs. *Chem.—Eur. J.* **2020**, *26*, 16793−16801. Thianthrenes: (f) Ren, T.; Xiao, J.; Wang, W.; Xu, W.; Wang, S.; Zhang, X.; Wang, X.; Chen, H.; Zhao, J.; Jiang, L. Synthesis, Crystal Structures, Optical Properties, and Photocurrent Response of Heteroacene Derivatives. *Chem.—Asian J.* **2014**, *9*, 1943−1949. (g) Dong, S.; Herng, T. S.; Gopalakrishna, T. Y.; Phan, H.; Lim, Z. L.; Hu, P.; Webster, R. D.; Ding, J.; Chi, C. Extended Bis(benzothia)-quinodimethanes and Their Dications: From Singlet Diradicaloids to Isoelectronic Structures of Long Acenes. *Angew. Chem., Int. Ed.* **2016**, *55*, 9316−9320.

(9) Brend'amour, S.; Gilmer, J.; Bolte, M.; Lerner, H.-W.; Wagner, M. C-Halogenated 9,10-Diboraanthracenes: How the Halogen Load and Distribution Influences Key Optoelectronic Properties. *Chem.—Eur. J.* **2018**, *24*, 16910−16918.

(10) Beck, J.; Bredow, T.; Tjahjanto, R. T. Thianthrene Radical Cation Hexafluorophosphate. *Z. Naturforsch., B: J. Chem. Sci.* **2009**, *64*, 145−152.

(11) Connelly, N. G.; Geiger, W. E. Chemical Redox Agents for Organometallic Chemistry. *Chem. Rev.* **1996**, *96*, 877−910.

(12) (a) Munakata, M.; Yan, S. G.; Ino, I.; Kuroda-Sowa, T.; Maekawa, M.; Suenaga, Y. Synthesis and Structure of a Novel Bis(μ-η^2-thianthrene)disilver(I) Bis(Perchlorate). *Inorg. Chim. Acta* **1998**, *271*, 145−150. (b) Amthor, S.; Lambert, C.; Graser, B.; Leusser, D.; Selinka, C.; Stalke, D. Synthesis and Ligand Properties of Thianthrenophane. *Org. Biomol. Chem.* **2004**, *2*, 2897−2901. (c) Triandi, R.; Beck, J. Synthesis and Crystal Structures of Silver Thianthrene Complexes with Weakly Coordinating Anions. *Z. Naturforsch., B: J. Chem. Sci.* **2007**, *62*, 1291−1297.

(13) John, A.; Bolte, M.; Lerner, H.-W.; Wagner, M. A Vicinal Electrophilic Diborylation Reaction Furnishes Doubly Boron-Doped Polycyclic Aromatic Hydrocarbons. *Angew. Chem., Int. Ed.* **2017**, *56*, 5558−5592.

(14) Ong, W. J.; Swager, T. M. Dynamic Self-Correcting Nucleophilic Aromatic Substitution. *Nat. Chem.* **2018**, *10*, 1023−1030.

(15) Kaehler, T.; John, A.; Jin, T.; Bolte, M.; Lerner, H. W.; Wagner, M. Selective Vicinal Diiodination of Polycyclic Aromatic Hydrocarbons. *Eur. J. Org. Chem.* **2020**, *2020*, 5847−5851. Note that carbonate salts in the presence of (trace amounts of) H_2O are employed in Suzuki-type coupling reactions to achieve B−C-bond cleavage. Thus, corresponding reaction conditions are best avoided when the substrate contains BAr_3 groups: (a) Wang, N.; Hudson, Z. M.; Wang, S. Reactivity of Aryldimesitylboranes under Suzuki−Miyaura Coupling Conditions. *Organometallics* **2010**, *29*, 4007−4011. (b) Reference 8a.

(16) Herzog, U.; Böhme, U.; Rheinwald, G. 1,2-Dithiolate Derivatives of Monosilanes and Disilanes. *J. Organomet. Chem.* **2000**, *612*, 133−140.

(17) Park, N. H.; dos Passos Gomes, G.; Fevre, M.; Jones, G. O.; Alabugin, I. V.; Hedrick, J. L. Organocatalyzed Synthesis of Fluorinated Poly(aryl thioethers). *Nat. Commun.* **2017**, *8*, 166.

(18) THF is also a suitable solvent. An advantage is that shorter reaction times are required. A disadvantage is the better solubility of the compounds compared to C_6H_6, which makes purification more tedious. Furthermore, we preferred to strictly avoid donor solvents, as they might affect the optoelectronic characterization of the products.

(19) The Si−F bond-dissociation energy (142 kcal mol^{-1} at 298 K) is among the highest of all element−element single bonds: Holleman, A. F.; Wiberg, N. *Lehrbuch der Anorganischen Chemie*; de Gruyter: Berlin, New York, 1995; Vol. 101, p 141.

(20) See the Supporting Information for more details.

(21) Kirschner, S.; Mewes, J.-M.; Bolte, M.; Lerner, H.-W.; Dreuw, A.; Wagner, M. How Boron Doping Shapes the Optoelectronic Properties of Canonical and Phenylene-Containing Oligoacenes: A Combined Experimental and Theoretical Investigation. *Chem.—Eur. J.* **2017**, *23*, 5104−5116.

(22) Jameson, C. J.; Mason, J. *Multinuclear NMR*; Plenum Press: New York, 1987; pp 221−258.

(23) Gallaher, K. L.; Bauer, S. H. Structure and Inversion Potential of Thianthren. *J. Chem. Soc., Faraday Trans.* **1975**, *71*, 1173−1182.

(24) Larson, S. B.; Simonsen, S. H.; Martin, G. E.; Smith, K.; Puig-Torres, S. Structures of Thianthrene (I), $C_{12}H_8S_2$, (Redeterminations at 163 K and 295 K) and 1-Azathianthrene (II), $C_{11}H_7NS_2$, (at 163 K). *Acta Crystallogr., Sect. C: Cryst. Struct. Commun.* **1984**, *40*, 103−106.

(25) Deubel, D. V. Thianthrene 5-Oxide as a Probe for the Electronic Character of Oxygen-Transfer Reactions: Re-interpretation of Experiments Required. *J. Org. Chem.* **2001**, *66*, 2686−2691.

(26) A ladder-type heteraborin with heptacene-type structure containing three incorporated B and three incorporated S atoms has been reported: Agou, T.; Kobayashi, J.; Kawashima, T. Electronic and Optical Properties of Ladder-Type Heteraborins. *Chem.—Eur. J.* **2007**, *13*, 8051−8060. The optoelectronic properties of the compound are not directly comparable with those of our B,S-doped PAHs, because the measurements have been performed in the significantly less polar solvent *c*-hexane

(27) Richardson, D. E.; Taube, H. Determination of E_2°-E_1° in Multistep Charge Transfer by Stationary-Electrode Pulse and Cyclic Voltammetry: Application to Binuclear Ruthenium Ammines. *Inorg. Chem.* **1981**, *20*, 1278−1285.

(28) Bock, H.; Rauschenbach, A.; Näther, C.; Kleine, M.; Havlas, Z. Thianthren-Radikalkation-Tetrachloroaluminat. *Chem. Ber.* **1994**, *127*, 2043−2049.

(29) (a) The salt [TA][PF_6] is only sparingly soluble in CH_2Cl_2. More reliable CV data are thus obtained in MeCN. Since DBAs tend to form (weak) adducts with MeCN (ref 20), we refrained from using this solvent for our own CV measurements. Fortunately, the oxidation potential of TA does not seem to be strongly solvent dependent (ref 10). (b) The average S−C-bond lengths to the peripheral *ortho*-phenylene rings *versus* the C_6-rings carrying B atoms are 1.769 *versus* 1.765 Å (**2**), 1.774 *versus* 1.761 Å (**3**), and 1.775 *versus* 1.780 Å (**4**) Systematic differences in the S−C double-bond character are not evident.

(30) Due to its higher boiling point, 1,2-$C_2H_4Cl_2$ was used as the solvent instead of CH_2Cl_2 in our SCE measurements, which resulted in only very minor shifts of the absorption bands. The irradiation of the sample and the electrochemical processes taking place lead to a considerable heat input into the thin-layer electrolysis cell. In a low-boiling solvent, the formation of bubbles can lead to loss of electrical contact and mixing in the diffusion layer, which is detrimental to the measurement.

(31) De Sorgo, M.; Wasserman, B.; Szwarc, M. Aggregation of Salts of Thianthrene Radical Cations. *J. Phys. Chem.* **1972**, *76*, 3468−3471.

(32) Krejčik, M.; Daněk, M.; Hartl, F. Simple Construction of an Infrared Optically Transparent Thin-Layer Electrochemical Cell: Applications to the Redox Reactions of Ferrocene, $Mn_2(CO)_{10}$ and $Mn(CO)_3$(3,5-di-t-butyl-catecholate)$^-$. *J. Electroanal. Chem.* **1991**, *317*, 179−187.

(33) (a) Fava, A.; Sogo, P. B.; Calvin, M. Chemistry and Spin Resonance Spectroscopy of Radicals from Thioaromatic Compounds. *J. Am. Chem. Soc.* **1957**, *79*, 1078−1083. (b) Shine, H. J.; Dais, C. F.; Small, R. J. Ion Radicals. IV. The Electron Spin Resonance Spectra of Substituted Thianthrenes in Sulfuric Acid Solution. *J. Org. Chem.* **1964**, *29*, 21−25.

(34) The appearance of bathochromically shifted Vis bands upon one-electron reduction of DBAs has been published: (a) Hoffend, C.;

Schödel, F.; Bolte, M.; Lerner, H.-W.; Wagner, M. Boron-Doped Tri(9,10-anthrylene)s: Synthesis, Structural Characterization, and Optoelectronic Properties. *Chem.—Eur. J.* **2012**, *18*, 15394−15405. (b) Hoffend, C.; Diefenbach, M.; Januszewski, E.; Bolte, M.; Lerner, H.-W.; Holthausen, M. C.; Wagner, M. Effects of Boron Doping on the Structural and Optoelectronic Properties of 9,10-Diarylanthracenes. *Dalton Trans.* **2013**, *42*, 13826−13837. (c) Hoffend, C.; Schickedanz, K.; Bolte, M.; Lerner, H.-W.; Wagner, M. Functionalization of Boron-Doped Tri(9,10-anthrylene)s. *Tetrahedron* **2013**, *69*, 7073−7081.

(35) Krossing, I. The Facile Preparation of Weakly Coordinating Anions: Structure and Characterisation of Silverpolyfluoroalkoxyaluminates $AgAl(OR_F)_4$, Calculation of the Alkoxide Ion Affinity. *Chem.—Eur. J.* **2001**, *7*, 490−502.

(36) HypSpec software. http://www.hyperquad.co.uk/HypSpec.htm (accessed May 24, 2022); (b) Gans, P.; Sabatini, A.; Vacca, A. Investigation of Equilibria in Solution. Determination of Equilibrium Constants with the HYPERQUAD Suite of Programs. *Talanta* **1996**, *43*, 1739−1753.

(37) Since our DFT-calculations on the Ag^+ complexation of **1** gave excellent agreement with the experimentally obtained electronic spectra already for the simpler 2:2 complex $[Ag_2\mathbf{1}_2]^{2+}$, we regard this species as a realistic model to describe the effects of Ag^+ ions on the optoelectronic properties of B,S-PAH **1**.

(38) (a) Job, P. Formation and Stability of Inorganic Complexes in Solution. *Ann. Chim.* **1928**, *9*, 113−203. (b) Hill, Z. D.; MacCarthy, P. Novel approach to Job's method: An undergraduate experiment. *J. Chem. Educ.* **1986**, *63*, 162−167. (c) Thordarson, P. Determining Association Constants from Titration Experiments in Supramolecular Chemistry. *Chem. Soc. Rev.* **2011**, *40*, 1305−1323.

(39) Renny, J. S.; Tomasevich, L. L.; Tallmadge, E. H.; Collum, D. B. Method of Continuous Variations: Applications of Job Plots to the Study of Molecular Associations in Organometallic Chemistry. *Angew. Chem., Int. Ed.* **2013**, *52*, 11998−12013.

(40) This statement is based on the following facts: (i) according to NMR spectroscopy, product **1** was pure (see Figures S1−S3). The concentration of the contaminating molecule is thus beyond the detection limit of the NMR spectrometer. (ii) The ratio between the shoulder and the main band decreased upon repeated column chromatography/recrystallization (but never vanished completely; see Figure S17a). (iii) The emission maximum of **SM1** is λ_{max} = 513 nm (CH_2Cl_2). Furthermore, **SM1** (Φ_{PL} = 86%; *c*-hexane) is much more fluorescent than **1** (Φ_{PL} = 12%; CH_2Cl_2). (iv) An excitation spectrum recorded at λ = 513 nm did not reproduce the absorption spectrum of **1**.

(41) Runge, E.; Gross, E. K. U. Density-Functional Theory for Time-Dependent Systems. *Phys. Rev. Lett.* **1984**, *52*, 997−1000.

(42) (a) Baer, R.; Livshits, E.; Salzner, U. Tuned Range-Separated Hybrids in Density Functional Theory. *Annu. Rev. Phys. Chem.* **2010**, *61*, 85−109. (b) Rohrdanz, M. A.; Martins, K. M.; Herbert, J. M. A Long-Range-Corrected Density Functional That Performs Well for Both Ground-State Properties and Time-Dependent Density Functional Theory Excitation Energies, Including Charge-Transfer Excited States. *J. Chem. Phys.* **2009**, *130*, 054112.

(43) (a) Mewes, J. M.; Herbert, J. M.; Dreuw, A. On the Accuracy of the General, State-Specific Polarizable-Continuum Model for the Description of Correlated Ground- and Excited States in Solution. *Phys. Chem. Chem. Phys.* **2017**, *19*, 1644−1654. (b) Mewes, J. M.; You, Z. Q.; Wormit, M.; Kriesche, T.; Herbert, J. M.; Dreuw, A. Experimental Benchmark Data and Systematic Evaluation of Two a Posteriori, Polarizable-Continuum Corrections for Vertical Excitation Energies in Solution. *J. Phys. Chem. A* **2015**, *119*, 5446−5464.

(44) Note that vibrational couplings have not been included in our calculations such that vibrational progressions, for example, that of the most bathochromic absorption of **1**, are not reproduced.

(45) Wavelengths in [nm] are calculated from the rounded energy values in [eV] as given in the main text.

(46) (a) Szakács, Z.; Glöcklhofer, F.; Plasser, F.; Vauthey, E. Excited-State Symmetry Breaking in 9,10-Dicyanoanthracene-Based Quadrupolar Molecules: the Effect of Donor-Acceptor Branch Length. *Phys. Chem. Chem. Phys.* **2021**, *23*, 15150−15158. (b) Dereka, B.; Svechkarev, D.; Rosspeintner, A.; Aster, A.; Lunzer, M.; Liska, R.; Mohs, A. M.; Vauthey, E. Solvent Tuning of Photochemistry upon Excited-State Symmetry Breaking. *Nat. Commun.* **2020**, *11*, 1925. (c) Szakács, Z.; Vauthey, E. Excited-State Symmetry Breaking and the Laporte Rule. *J. Phys. Chem. Lett.* **2021**, *12*, 4067−4071.

(47) Kutzelnigg, W.; Fleischer, U.; Schindler, M. The IGLO Method: Ab initio Calculation and Interpretation of NMR Chemical Shifts and Magnetic Susceptibilities. *Deuterium and Shift Calculation*; NMR Basic Principles and Progress; Springer: Berlin, Heidelberg, 1991; Vol. *23*, pp 165−262.

(48) Grimme, S. Accurate Calculation of the Heats of Formation for Large Main Group Compounds with Spin-Component Scaled MP2 Methods. *J. Phys. Chem. A* **2005**, *109*, 3067−3077.

(49) Witwicki, M.; Walencik, P. K.; Jezierska, J. How Accurate Is Density Functional Theory in Predicting Spin Density? An Insight from the Prediction of Hyperfine Coupling Constants. *J. Mol. Model.* **2020**, *26*, 10.

(50) Stoll, S.; Schweiger, A. EasySpin, a Comprehensive Software Package for Spectral Simulation and Analysis in EPR. *J. Magn. Reson.* **2006**, *178*, 42−55.

(51) (a) Bannwarth, C.; Ehlert, S.; Grimme, S. GFN2-xTB-An Accurate and Broadly Parametrized Self-Consistent Tight-Binding Quantum Chemical Method with Multipole Electrostatics and Density-Dependent Dispersion Contributions. *J. Chem. Theory Comput.* **2019**, *15*, 1652−1671. (b) Pracht, P.; Bohle, F.; Grimme, S. Automated Exploration of the Low-Energy Chemical Space with Fast Quantum Chemical Methods. *Phys. Chem. Chem. Phys.* **2020**, *22*, 7169−7192.

(52) Grimme, S.; Hansen, A.; Ehlert, S.; Mewes, J. M. r2SCAN-3c: A "Swiss army knife" composite electronic-structure method. *J. Chem. Phys.* **2021**, *154*, 064103.

(53) Santra, G.; Sylvetsky, N.; Martin, J. M. L. Minimally Empirical Double-Hybrid Functionals Trained against the GMTKN55 Database: revDSD-PBEP86-D4, revDOD-PBE-D4, and DOD-SCAN-D4. *J. Phys. Chem. A* **2019**, *123*, 5129−5143.

(54) Marenich, A. V.; Cramer, C. J.; Truhlar, D. G. Universal Solvation Model Based on Solute Electron Density and on a Continuum Model of the Solvent Defined by the Bulk Dielectric Constant and Atomic Surface Tensions. *J. Phys. Chem. B* **2009**, *113*, 6378−6396.

(55) At first glance, it seems surprising that the entropic penalty for $[Ag_2\mathbf{1}_3]^{2+}$ is much smaller than for the sandwich dimer, since the number of bonded molecules (and thus the loss of translational and rotational degrees of freedom) is larger in $[Ag_2\mathbf{1}_3]^{2+}$. However, a breakdown of the entropic contributions shows that these translations and rotational effects are overcompensated by vibrational contributions. We argue that in the sandwich dimer, many entropically relevant low-energy large-amplitude motions of the Mes and 2,3-anthrylene groups are constrained due to the close contact between them. In contrast, these groups are as unconstrained in $[Ag_2\mathbf{1}_3]^{2+}$ as in free **1** (compare the structures shown in Figure 6). This rationale is corroborated by the fact that the entropic penalty for the extended dimer, which has similarly unconstrained Mes/2,3-anthrylene groups as $[Ag_2\mathbf{1}_3]^{2+}$, is much smaller than for the sandwich dimer.

(56) For a comprehensive review on thoroughly characterized Ag^+ complexes of polycyclic aromatic hydrocarbons, see: Munakata, M.; Wu, L. P.; Ning, G. L. A new type of multilayer system-silver(I) complexes of polycyclic aromatic compounds. *Coord. Chem. Rev.* **2000**, *198*, 171−203.